



CFD simulation of the wind field over a terrain with sand fences: Critical spacing for the wind shear velocity

Izael A. Lima^{a,b}, Eric J.R. Parteli^b, Yaping Shao^c, José S. Andrade^a, Hans J. Herrmann^{a,d}, Ascânio D. Araújo^{a,*}

^a Departamento de Física, Universidade Federal do Ceará, Fortaleza, 60451-970 Fortaleza, Ceará, Brazil

^b Department of Geosciences, University of Cologne, Pohligstr. 3, 50969 Cologne, Germany

^c Institute for Geophysics and Meteorology, University of Cologne, Pohligstr. 3, 50969 Cologne, Germany

^d PMMH, ESPCI Paris, 7 quai St. Bernard, 75005 Paris, France

ARTICLE INFO

Keywords:

Wind erosion
Computational fluid dynamics
Sand fences
Soil protection

ABSTRACT

Sand fences are often erected to reduce wind speed, prevent aeolian soil focus our investigation on the behaviour of the near-surface wind shear velocity, which is defined here using a simple model based on wind speed values at height 20% of the fence height. Our simulations reveal novel insights about the three-dimensional structure of the turbulent wind flow between fences that are important for developing a theoretical description of this flow. We find that the area of soil associated with values of near-surface wind shear velocity that are below the minimal threshold for sand transport has two regimes, depending on the spacing L_x between the fences. When L_x is smaller than a critical value L_{xc} , the wake zones associated with each fence are inter-connected (regime A), while these wake zones appear separated from each other (regime B) when L_x exceeds this critical value of spacing. The system undergoes a second order phase transition at $L_x = L_{xc}$, with the cross-wind width of the protected zone scaling with $[1 - L_x/L_{xc}]^\beta$ in regime A, with $\beta \approx 0.32$. Moreover, we also perform a comparative investigation of arrays of constant and multiple fence heights on the basis of the two-dimensional shear velocity field obtained from our simulations. Our findings have implication for a better understanding of aeolian transport in the presence of sand fences, as well as to develop optimization strategies for measures to protect soils from wind erosion.

1. Introduction

Wind-blown sand is one important factor for the erosion of soils, the abrasion of rocks, the morphodynamics of ripples and dunes and the propagation of desertification. The most important transport mode of wind-blown sand grains is saltation, which consists of grains moving in nearly ballistic trajectories thereby ejecting new grains upon collision with the soil (splash) (Bagnold, 1941; Shao and Li, 1999; Almeida et al., 2006; Almeida et al., 2008; Shao, 2008; Carneiro et al., 2011; Carneiro et al., 2013; Pähz and Durán, 2018). The splash is also one of the main factors for the emission of dust (Shao et al., 1993; Shao, 2001; Lu and Shao, 1999), which, once entrained, may be transported over thousands of kilometers in suspension, thereby affecting climate and human health (Kok et al., 2012). Soil protection from aeolian erosion constitutes, thus, one aspect of broad implication for climate, environment and society.

To achieve soil protection from erosive winds, sand fences of

various types are constructed with the aim of reducing wind velocity and inducing sand accumulation and dune formation (Li and Sherman, 2015). Such fences typically consist of wire, lightweight wood strips or perforated plastic sheets attached to regularly spaced supports (Pye and Tsoar, 1990). Moreover, most sand fences are porous, as solid fences that completely block the wind may induce strong vortices extending up to several fence heights downwind, while a porous fence protects larger areas of leeward sheltered ground than its solid counterpart does (Cornelis and Gabriels, 2005; Bruno et al., 2018).

The objective the sand fence array is to reduce the wind velocity below the minimal value required for saltation transport, which is the main sediment transport mode causing aeolian soil erosion. In other words, soil erosion is caused at those places where the wind velocity is above this minimal threshold, which is of the order of 6 m/s (measured at a height of 1 m above the soil) but can be higher depending, for instance, on the presence of moisture or non-erodible elements on the soil (Pye and Tsoar, 1990; Tsoar, 2001; Kok et al., 2012). Moreover, soil

* Corresponding author.

E-mail address: ascanio@fisica.ufc.br (A.D. Araújo).

<https://doi.org/10.1016/j.aeolia.2020.100574>

Received 1 May 2019; Received in revised form 5 December 2019; Accepted 7 January 2020

1875-9637/ © 2020 Published by Elsevier B.V.

erosion is particularly strong at coastal and desert areas subjected to unidirectional sand-moving winds. While multidirectional wind regimes lead to accumulating dunes, unidirectional wind regimes cause the formation of migrating dunes (Wasson and Hyde, 1983).

The properties of three-dimensional turbulent wind flow over an array of fences are still poorly described. Their understanding is important to accurately predict wind erosion patterns in the presence of sand fences and to develop efficient strategies to protect sediment soils from aeolian erosion. While most of the previous investigations (Baltaxe, 1967; Wilson, 1987; Lee and Kim, 1999; Lee et al., 2002; Wu et al., 2013; Dong et al., 2006; Telenta et al., 2014; Zhang et al., 2015; Tsukahara et al., 2012; Savage, 1963; Nordstrom et al., 2012; Telenta et al., 2014; Hatanaka and Hotta, 1997; Alhajraf, 2004; Wilson, 2004; Bouvet et al., 2006; Santiago et al., 2007; Liu et al., 2014; Bitog et al., 2009) focused on the flow characteristics over a single fence, the air-flow over fence arrays consisting of 5–10 fences or more has been investigated, for instance, in wind-tunnel experiments (Guan et al., 2009) and Computational Fluid Dynamic simulations (Lima et al., 2017). Moreover, the simulations by Lima et al. (2017), which calculated the average turbulent wind flow in a two-dimensional cut along the symmetry axis of the fences, showed how maximal wind speeds occurring within the array depend on fence porosity, spacing and height. However, to more realistically model scenarios with fences of finite cross-width, three-dimensional simulations are required.

In the present work, we simulate the turbulent flow over a three-dimensional array of sand fences. Our aim is to investigate how the total area of the soil associated with values of wind shear velocity near the surface (defined in the next section) that are below the minimal threshold for sand transport depends on the main parameters of the system, i.e. fence porosity, height and spacing. In the present work, we focus on the structure of the average turbulent wind field over the terrain in presence of the sand fences, and in the absence of saltation or suspension transport. We note that the presence of sand grains in the transport layer alters the wind profile, as shown, for instance, by Xu et al. (2018). However, our main objective is to investigate how different arrays modify the soil area where the local wind velocity (in the absence of saltating grains) is reduced below the minimal threshold value for saltation transport. To define this area, we consider the average wind velocity close to the ground within the region between the fences.

Computational Fluid Dynamic simulations provide a helpful means to better assess the near-surface wind shear velocity field, which is affected by complex three-dimensional structures of the wind flow between the fences. Moreover, one of the challenges for optimizing aeolian soil protection consists in achieving maximal reduction of wind shear velocity with the smallest amount of material for fence construction and maintenance (Lima et al., 2017). In this manuscript, we thus provide comparative results for the two-dimensional field of near-surface shear velocity from simple arrays of fences (i.e., when the fence height and inter-fence spacing are constant over the field) with those from complex arrays of fences with multiple values of height and spacing. In the next section, we explain the numerical setup and the Computational Fluid Dynamic model employed in our calculations. (See Fig. 1).

2. Numerical experiments

Fig. 2 shows the schematic representation of the setup employed in our simulations. This consists of a three-dimensional channel of height $\Delta z = 10h_f$, width $\Delta y = 20h_f$ and length $\Delta x = 80h_f + 9L$, while the fences, each of height h_f , are erected vertically on the bottom wall of this channel at different values of inter-fence spacing L , as described later. The fences have a cross-wind width $W_f = 10h_f$, which is 50% of the lateral width Δy of the wind channel (Fig. 2). The soil level in the absence of the fences is constant and equal to zero, while the dimensions of the wind channel are chosen to be large enough to ensure that border



Fig. 1. Application of sand fences to prevent wind erosion—a field example. The image shows fences made of coconut leaves in Paracuru, near Fortaleza, main city of State of Ceará in Northeastern Brazil (photo by first authors, I.A.L. and A.D.A.).

effects can be neglected, but small enough for efficient numerical simulation. We have checked that the results, presented in the next section, remained unchanged by increasing the box dimensions. We use a full size model for the sand fences, i.e., our simulations are performed with heights $h_f = 50$ cm and 1 m which are consistent with values applied in field experiments of aeolian soil protection (Li and Sherman, 2015).

We consider that the fences are subjected to an average turbulent wind flow in x direction (cf. Fig. 2). In the absence of fences, the average horizontal wind velocity over the flat ground $\vec{u}(x, y, z)$ increases logarithmically with the height z above the bed level (Bagnold, 1941; Pye and Tsoar, 1990). To represent such average upwind flow condition in our calculations, the logarithmic velocity profile for $\vec{u}(x, y, z)$ is imposed as boundary condition at the simulation inlet. Specifically, at the horizontal position $x = 0$, $\vec{u}(0, y, z) = 0$ for $z = \delta$, where δ is the surface roughness. The horizontal velocity increases with z according to the following equation (which is valid for $z \geq \delta$) (Bagnold, 1941; Pye and Tsoar, 1990):

$$\vec{u}(0, y, z) = \frac{u_{*0}}{\kappa} \log \left[\frac{z}{\delta} \right] \vec{e}_x, \quad (1)$$

where \vec{e}_x is the unit vector pointing in the direction x , u_{*0} is the magnitude of the upwind shear velocity of the wind and $\kappa = 0.4$ is the von Kármán constant. The shear velocity u_{*0} is proportional to the mean flow velocity gradient in turbulent boundary layer flow, and is used to define the upwind shear stress,

$$\vec{\tau}_0 = \vec{\tau}(0, y) = [\rho_{\text{air}} u_{*0}^2] \vec{e}_x, \quad (2)$$

where $\rho_{\text{air}} = 1.225 \text{ kg/m}^3$ denotes the air density. Moreover, we take for the surface roughness the value $\delta = 100 \mu\text{m}$, which is within the range between $10 \mu\text{m}$ and 1.0 mm valid for flat sand covered surface (Pye and Tsoar, 1990). In our simulations, we apply a wind shear velocity $u_{*0} = 0.4 \text{ m/s}$, considering that sand-moving upwind shear velocities in dune fields can reach from the threshold for sustained saltation, i.e., $u_{*t} \approx 0.2 \text{ m/s}$, up to values of the order of 0.5 m/s (Sauermaun et al., 2003; Claudin et al., 2013). Moreover, much stronger wind velocities of the order of $4u_{*t}$ are not considered since above this value sand grains are transported in suspension (Pähtz et al., 2013).

In our calculations, each sand fence is modeled as a vertical, porous wall, implemented by a special type of boundary condition representing a porous membrane of a certain velocity/pressure drop characteristics (Wilson, 1985; Santiago et al., 2007; Araújo et al., 2009; Yeh et al., 2010). At height z , this pressure drop is given by the expression

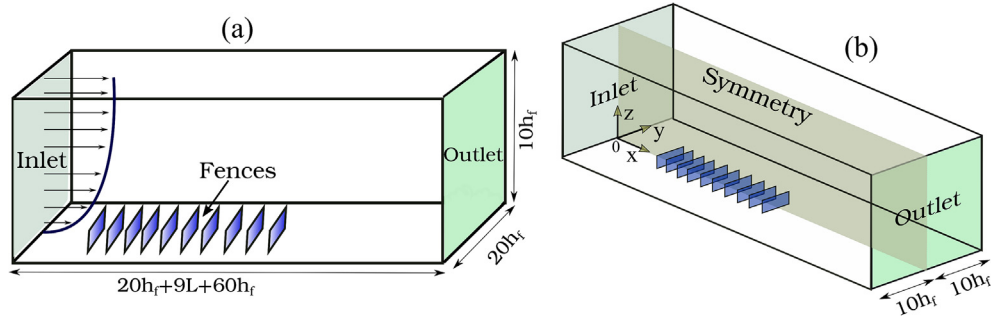


Fig. 2. Schematic diagram showing the geometry of the wind channel with the array of fences on its bottom. The fences have height h_f and between them a spacing L . At the inlet, the logarithmic profile for the wind velocity is imposed following Eq. (1).

$$\Delta p(x, y, z) = -\frac{1}{4\Phi^2} \rho_{\text{air}} [\vec{u}(x, y, z) \cdot \vec{e}_x]^2 \Delta m, \quad (3)$$

where the term in the brackets is the wind velocity normal to the fence, i.e., the horizontal wind speed at height z , Δm is the fence's thickness and Φ its porosity. The fences' thickness is set as $\Delta m = 10^{-4}$ m, while a nominal porosity of 20% (Li and Sherman, 2015; Lima et al., 2017) is used in our calculations.

We remark that our model does not resolve the pores, i.e. it is a continuum model where the pores are assumed to be uniformly distributed throughout the fence cross-sectional area. Accordingly, our model does not address the effect of the shape of the opening (pores). However, Li and Sherman (2015) summarized literature data on the effect of the shape and size of the pores, and showed that the effect of pore shape and size is non-trivial but small, and their impact is most often reflected in the changing characteristics of the turbulence in the immediate lee of a fence. The investigation of the shape of the opening and the arrangement of the pores certainly poses an interesting topic for future modeling.

Therefore, in our simulations, the fences have no holes. Instead, each fence is treated as a continuum medium to which a porosity is attributed. However, this porosity is not simulated geometrically in the simulation, i.e., we do not apply any physical method to explicitly represent pores of given shape or distribution. Instead, the fences are represented as an homogeneous surface, and the porosity appears in the mathematical expression associated with the fences (Eq. (3)), to compute the pressure drop from their upwind to their downwind side.

We consider that the fluid (air) is incompressible and Newtonian, while the calculation of the average turbulent wind field over the soil is performed as described in previous works (Herrmann et al., 2005; Araújo et al., 2013). Specifically, the Reynolds-averaged Navier-Stokes equations are solved using the FLUENT Inc. commercial package (version 14.5.7), in which the standard $\kappa - \epsilon$ model is applied in the computations to simulate turbulence. The time-averaged (or Reynolds-averaged) Navier-Stokes equations for the wind flow over the terrain are solved in the fully-developed turbulent regime. In the calculations, a non-slip boundary condition is applied to the fluid-solid interface defined by the soil and the fences, while at the top wall, the shear stress of the wind is set equal to zero (Herrmann et al., 2005; Almeida et al., 2006, 2008; Araújo et al., 2013; Michelsen et al., 2015; Lima et al., 2017). Since the fences have a finite cross-wind width $W_f = 0.5 \cdot \Delta y$ (see Fig. 2), to avoid border effects and to resolve the flow in the region around the edges of the fences, both edges of the fence array are separated from the lateral walls by a distance equal to half the fence width (see Fig. 2). Given the symmetry of the system, and for the sake of computational efficiency, a symmetric boundary condition is applied in the y direction, with symmetry plane $y = 0$. The flow equations are, thus, solved for the right half of the simulation domain, and the developed solution mirrored along the symmetry plane $y = 0$ to obtain the flow field on the left half. Both lateral walls are treated as full slip walls, i.e., having zero shear stress.

Moreover, the default pressure-velocity coupling scheme ("SIMPLE") of the solver, which obtains a correction in the static pressure field to satisfy the continuity equation (Patankar and Spalding, 1972), is applied with its preselected values of parameters. At the outlet, a static pressure $P = 0$ is specified, while the default option "standard wall functions" of the solver is selected (Araújo et al., 2013; Lima et al., 2017). This option applies the wall boundary conditions to all variables of the $k - \epsilon$ model that are consistent with Eq. (1) along the channel's bottom wall (Lauder and Spalding, 1974).

To perform the calculations, a second-order upwind discretization scheme is applied to the momentum, whereas for the turbulent kinetic energy and turbulence dissipation rate we apply a first-order upwind scheme (Araújo et al., 2013). A rectangular grid with mean spacing of about 0.05 m is used for the lower region from the bottom wall ($z = 0$) up to the height of the fences ($z = h_f$), while for larger heights, a coarser grid is considered. Specifically, the grid cell size is 0.10 m within the range $h_f \leq z < 2h_f$ and 0.50 m for $2h_f < z \leq 10h_f$ (i.e. up to the top wall). Previous studies (Araújo et al., 2013; Lima et al., 2017) have shown little change in the flow profile by decreasing cell size below the aforementioned values, while too large cell sizes affect the convergence of the solution. However, we remark that an interesting point for future work is the investigation of how different meshes affect surface roughness and flow convergence. Such an investigation could be conducted, for instance, by explicitly accounting for mesh elements at the inlet, such as in previous wind tunnel experiments (Xu et al., 2018).

Moreover, the following initial conditions are applied: for all values of x, y, z , the velocity and the pressure are set to zero, while at the left wall ($x = 0$), the logarithmic profile Eq. (1) is imposed. Convergence of the numerical solution of the transport equations is evaluated in terms of residuals, which provide a measure for the degree up to which the conservation equations are satisfied throughout the flow field. Here, convergence is achieved when the normalized residuals for both ϵ and k fall below 10^{-4} , and when the normalized residuals for all three velocity components (in the directions x, y and z) fall below 10^{-6} . These values provide a compromise between accuracy and computational efficiency, as discussed in our previous work (Araújo et al., 2013; Lima et al., 2017). Specifically, we have performed simulations with smaller threshold values for the respective normalized residuals, and observed no significant changes in the results, discussed next.

Our numerical method has been verified in previous work in the context of sediment transport modeling and wind flow over sand dunes (Herrmann et al., 2005; Schatz and Herrmann, 2006; Almeida et al., 2006, 2008; Araújo et al., 2013), in which we have used the same solver that is applied in the present study. However, to verify the fence model we use in the solver, we compute the mean turbulent wind field over a terrain with fences using the same parameters as in the experiments by Guan et al. (2009), i.e., fences of height $h_f = 80$ mm, porosity of 50% and spacing of $20h_f$. As we can see in Fig. 3, we find reasonable quantitative agreement between our numerical predictions for the height profile of the mean downwind flow speed, $u_x(z)$, and the experimental observations by Guan et al. (2009) within the array. This

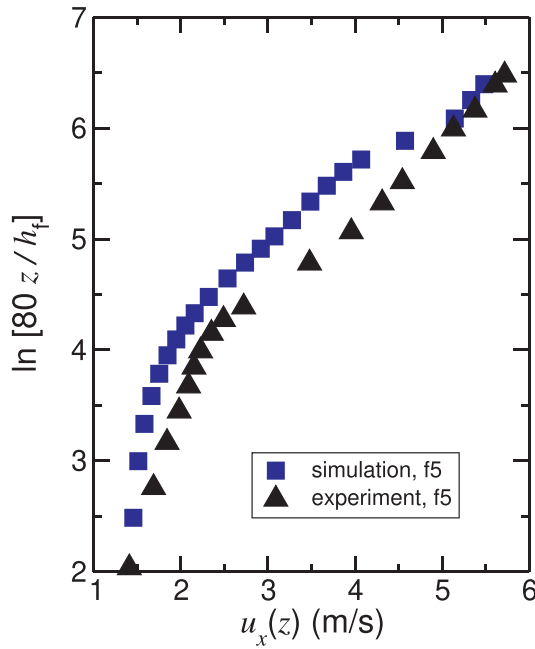


Fig. 3. To verify our model, we consider the setup employed in the controlled wind-tunnel experiments by Guan et al. (2009), i.e., 7 fences of height $h_f = 80$ mm and porosity of 50%, with inter-fence spacing and surface roughness amounting to $20h_f$ and 3 mm, respectively (Guan et al., 2009). Squares denote our numerical predictions for the vertical profile of the horizontal wind velocity, $u_x(z)$, as a function of z/h_f , measured along the array's symmetry axis at half distance between the fifth and sixth fences, i.e., near the end of the array. Triangles denote the corresponding experimental values (Guan et al., 2009).

agreement is remarkable considering that in our simulations, porosity is homogeneously distributed throughout fence area, while Guan et al. (2009) employed irregularly manufactured objects to model trees with optical porosity of 50%. Moreover, we also compute the longitudinal wind velocity profile for heights above the windbreaks and we find that, in this region, far downwind within the array of fences, the wind speed decreases with distance downwind, which is in agreement with wind-tunnel measurements (Guan et al., 2009). Moreover, as shown in Section 3, we also find that the maximal value of near-surface wind velocity between two fences in the array increases with distance downwind, which is also consistent with experiments Guan et al. (2009). In the sections which follow, we will further discuss in more detail the validity and significance of our results in the light of these experimental observations.

3. Results and discussion

Fig. 4 shows flow streamlines over an array of 10 fences of height $h_f = 0.5$ m, spacing $L_x = 20h_f = 10$ m and two values of porosity: $\phi = 20\%$ (upper panel in Fig. 4), and $\phi = 40\%$ (lower panel in Fig. 4). In our simulations, the cross-wind width of the fences is $W_f = 5$ m. The wind shear velocity upwind of the fences, u_{*0} , is 0.4 m/s, and its direction is indicated by the arrow in Fig. 4. In the three-dimensional simulation shown in Fig. 4 for the porosity $\phi = 20\%$ (Fig. 4a–c), we see the occurrence of flow recirculation on the horizontal plane, which is not visible in the simulation results for $\phi = 40\%$ (Fig. 4d–f). This is consistent with experimental and field observations of enhanced turbulence and occurrence of whirls for very low values of porosity (Li and Sherman, 2015). The porosity $\phi = 40\%$ is within the range of fence porosities that have proven to be most efficient in reducing flow pressure and turbulent kinetic energy over the sheltered terrain, i.e., $30\% < \phi < 50\%$ (Lee and Lim, 2001; Park and Lee, 2003; Li and Sherman, 2015).

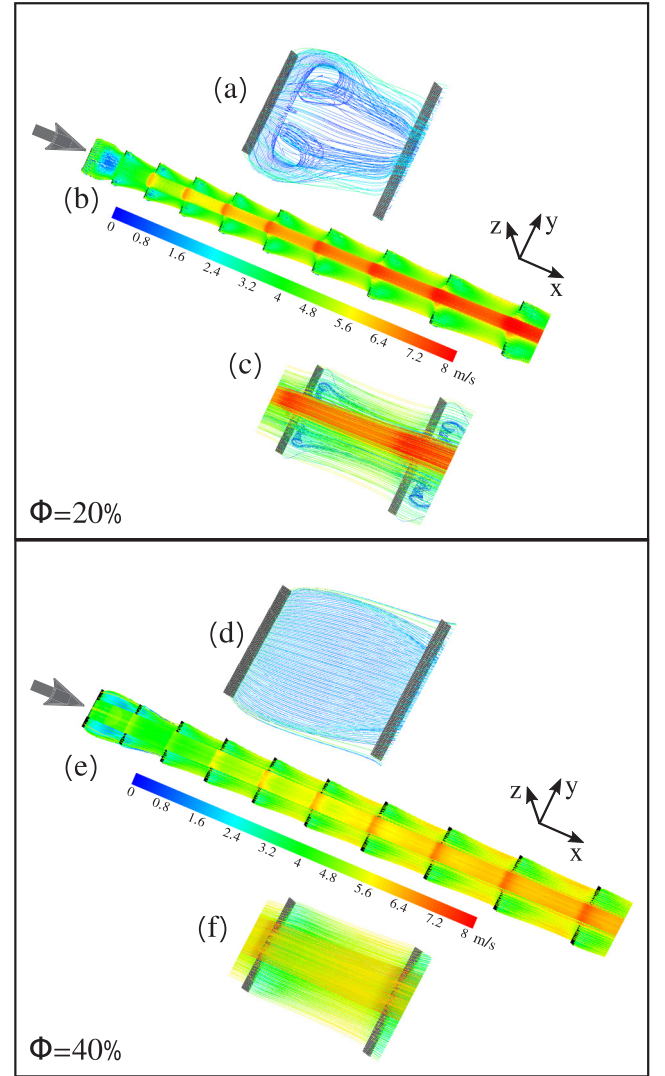


Fig. 4. Streamlines of the average turbulent wind flow over an array of 10 fences, obtained for porosity $\phi = 20\%$ (top) and $\phi = 40\%$ (bottom). The streamlines over the entire array obtained with these two porosity values are shown in (b) and (e), respectively. In (a) and (d) we see the respective streamlines for the first pair of fences, while (c) and (f) denote the corresponding results for the last two fences. The arrow at left in each panel indicates the wind direction. The colors indicate the magnitude of the wind velocity in m/s. Upwind shear velocity of the wind is $u_{*0} = 0.4$ m/s and fence height is 50 cm, while fence spacing is 5 m. The wind shear velocity has been calculated at height $z = 10$ cm.

3.1. Longitudinal profile of the wind shear velocity near the surface

Guan et al. (2009) introduced a simple airflow model to characterize the average turbulent wind flow over the soil in the region between porous fences, based on two-dimensional simulations. These authors defined the near-surface wind shear velocity from the reduction in the horizontal wind velocity $u_x(x)/u_x(x=0)$ at the reference height of $0.2h_f$. In the present work, we follow definition of Guan et al. (2009) for near-surface wind shear velocity to calculate, for different longitudinal slices of the system, i.e., slices in the direction of the wind, the wind shear velocity $u_{*x}(x, y)$ as a function of the downwind position x close to the ground. Therefore, following the experimental work by Guan et al. (2009), we use the relation

$$u_{*x}(x, y) \approx u_{*0} r(x, y), \quad (4)$$

where the two-dimensional field $r(x, y)$ is defined as

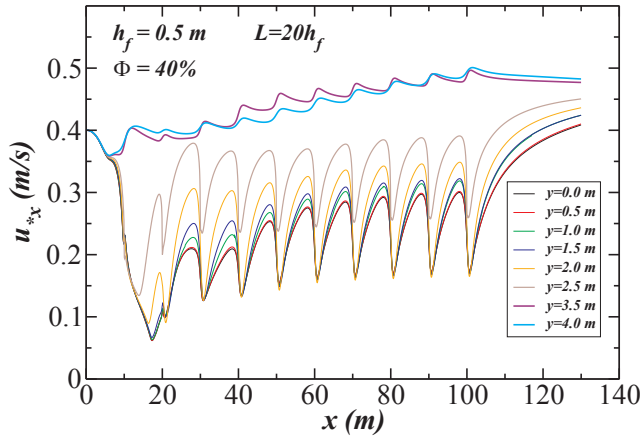


Fig. 5. Average longitudinal component of the wind shear velocity, u_{*x} , calculated using Eq. (4), as a function of the downwind position x for different values of y . The first fence is at $x = 10$ m, the last one at $x = 100$ m and the spacing is $L_x = 10$ m. Fence porosity is 40%, fence cross-wind width is 5 m and fence height is 50 cm, while the upwind shear velocity is $u_{*0} = 0.4$ m/s.

$r(x, y) \equiv u_x(x, y, z = 0.2h_f)/u_x(0, y, z = 0.2h_f)$, with $u_x(x, y, z) = \vec{u}(x, y, z) \cdot \vec{e}_x$ denoting the longitudinal component of the wind velocity. $r(x, y)$ gives the attenuation in the longitudinal wind velocity due to the presence of the fences, computed at a height of $z = 0.2h_f$ above the soil at the position (x, y) . By doing so, we obtain the results shown in Fig. 5, which correspond to the same parameter values of the simulation in Fig. 4.

We see in Fig. 5 that u_{*x} in the region between the fences near the symmetry axis of the system ($y = 0$) is reduced by a substantial amount. In particular, between the last two fences in the system, the maximal value of u_{*x} at $y = 0$ is about 63% of the upwind shear velocity u_{*0} . Moreover, u_{*x} increases with the lateral position towards the flanks of the fences. The two uppermost curves in Fig. 5 correspond to values of $|y| > 2.5$ m, that is beyond the lateral borders of the fences. We see that in this outer region, the near-surface wind shear velocity u_{*x} , computed from Eq. (4), is largest thereby exceeding the upwind value u_{*0} after the third fence. This result can be understood by noting that the fence array imposes an obstacle for the wind, and that there is thus a pressure reduction at the lateral border of the fence array. This pressure reduction is associated with the conservation of momentum of the fluid flow in the system, which leads to an increase in wind velocity near the flanks of the fence array.

Moreover, we see in Fig. 6 that the behavior of u_{*x} along the flanks

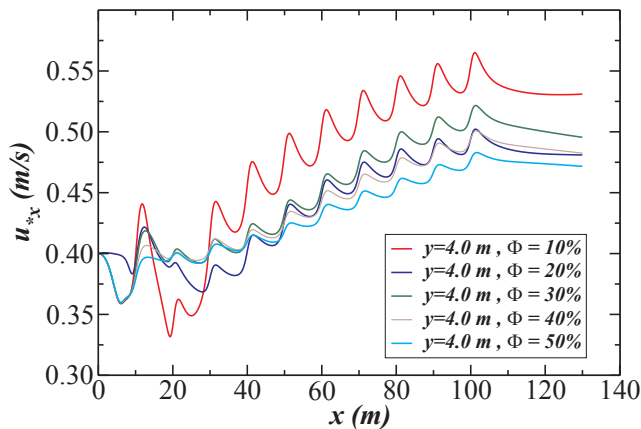


Fig. 6. Average longitudinal component of the wind shear velocity, u_{*x} , calculated using Eq. (4), as a function of the downwind position x for $y = 4$ m and different values of porosity ϕ . Fence positions and sizes are as in Fig. 5. Moreover, the upwind shear velocity is $u_{*0} = 0.4$ m/s.

of the fence array depends on the fence porosity ϕ . The increase in flow velocity at the lateral borders is stronger the lower the porosity, since the pressure drop at the sides of the fence array is stronger the less permeable the fences. We note that the objective of the analysis in Fig. 6 is to investigate the effect of the porosity on the local u_{*x} near the flanks of the fences. To this end, we evaluate in Fig. 6 the behavior of u_{*x} along the longitudinal slice $y = 4$ m, which has been chosen here since it is still close to the fence flanks but far enough from the lateral border of the channel.

3.2. Two-dimensional field of near-surface wind shear velocity u_{*x} (Eq. (4))

One important aspect of a sand fence array is its efficiency to protect soil against motion of sand grains. Since the impact of sand particles on the ground during saltation causes dust emission (Shao et al., 1993), soil protection against sand transport has implications not only for the dynamics of sand encroachment and aeolian desertification, but also for the Earth's climate and atmosphere. However, the complex structures of the wind flow near the ground in the region between the fences are still poorly understood. Here we compute the two-dimensional field of the average near-surface wind shear velocity u_{*x} (using Eq. (4)) in the presence of the fences, with the aim of investigating the total amount of area associated with near-surface shear velocity values below the minimal threshold for saltation.

Fig. 7 shows the two-dimensional field $u_{*x}(x, y)$, i.e., the values of u_{*x} as a function of the horizontal position. The blue area in the figure represents the wake region within the fence array, i.e., values of $u_{*x}(x, y)$ smaller than 0.25 m/s, which is approximately the minimal threshold shear velocity for direct entrainment of sand particles by fluid forces (Bagnold, 1941). We see in Fig. 7 that the shape of the wake region changes with distance downwind. For the first upwind fences, wake zones produced by the adjacent fences appear connected to each other, but they disconnect after the fourth fence.

Moreover, the shape of the wake zones as a function of the downwind distance, as well as the downwind position where the wake zones separate from each other, depend on several parameters of the system, such as upwind flow velocity u_{*0} , inter-fence distance L_x , fence porosity ϕ and number of fences in the array. Fig. 8 shows how the wake zones depend on the spacing between the fences. This figure shows that, for $u_{*0} = 0.4$ m/s, $\phi = 40\%$ and 10 fences, separation of the different wake zones of the fences starts after a certain value of spacing which is within the range $15 < L_x/h_f < 20$.

We investigate this behavior in more detail by varying the fence porosity and spacing (see Figs. 9a-c). The fence height is constant and equal to 50 cm, while the upwind flow shear velocity is 0.4 m/s (Lima et al., 2017). Each one of Fig. 9a-c shows the total protected area S , for which $u_{*x} < u_{*t}$ ($= 0.25$ m/s), as a function of the fence number i . This area S is measured from the mid positions between the two neighbouring fences, that is,

$$S = \int_{-0.5\Delta_y}^{0.5\Delta_y} \int_{x_i-0.5L_x}^{x_{i+1}+0.5L_x} \Theta(u_{*x}(x, y) - u_{*t}) dx dy \quad (5)$$

where $\Theta(x)$ is the Heaviside function, i.e. $\Theta(x) = 0$ for $x \leq 0$ and unity otherwise, while Δ_y is the cross-wind width of the channel and L_x the fence spacing.

For a spacing of $10h_f$ (Fig. 9a), we see that, for all porosity values from 10% to 50%, the wake region consists of interconnected wake zones forming a protected soil region of approximately constant shape and size throughout the fence array. This behavior leads to an approximately constant value of S associated with each fence, although for very high porosities the flow through the last fences tends to recover upwind conditions earlier, thus leading to a drop in the value of S . By taking a larger value for the fence spacing (cf. Fig. 9b; $L_x = 15h_f$), the fence wake zones appear inter-connected in the beginning of the array (up to the fourth fence). We see that, in this initial region, the value of S is

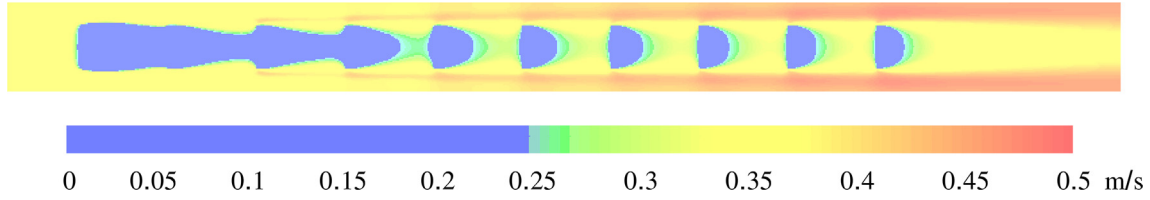


Fig. 7. Longitudinal component of the wind shear velocity field, u_{sx} , calculated using Eq. (4), for the array of fences in Fig. 5. The colors indicate the values of u_{sx} in m/s. The wind shear velocity has been calculated at height $z = 10$ cm using Eq. (4). (For interpretation of the references to colour in this figure legend, the reader is referred to the web version of this article.)

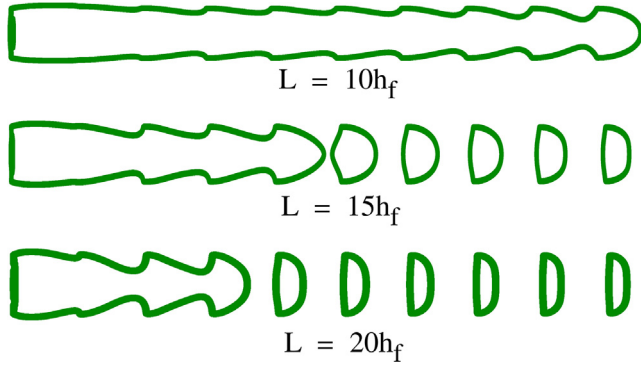


Fig. 8. Contour plot of the protected soil area, i.e. the area within which $u_{sx} < u_{ft}$ ($= 0.25$ m/s), for different spacings between the fences. The other parameters are the same as in Fig. 5. The wind shear velocity has been calculated at height $z = 10$ cm using Eq. (4).

approximately the same for all values of porosity (see Fig. 9b). However, from the fourth fence onwards, the zones of u_{sx} below threshold become smaller due to the obstacle's permeability, and S starts to decrease downwind at a rate that increases with fence porosity. This behavior is associated with a thinning of the wake region with distance downwind as can be seen in Fig. 8).

Moreover, Fig. 9b shows that, for high enough porosities, S first decreases rapidly with distance downwind (between fences 4 and 6) and then slowly from the sixth fence onwards, thus indicating the approach to an asymptotic value for very large downwind distances. This asymptotic behavior corresponds to the regime of disconnected wake zones, which is achieved faster the larger the fence spacing (see Fig. 8). Furthermore, we calculate in Fig. 9c the value of S as a function of the fence position for a higher spacing of $20h_f$. Clearly, the spacing in these calculations is so large that a dependence of S on the porosity is observed from the very beginning of the array, i.e., S decreases faster downwind the larger ϕ . The separation of the wake zones produced by the fences occurs from the sixth fence onwards for all values of ϕ larger than 10%. Far downwind within the array, the system is found within the regime (or phase) of separated/ disconnected wake zones (regime

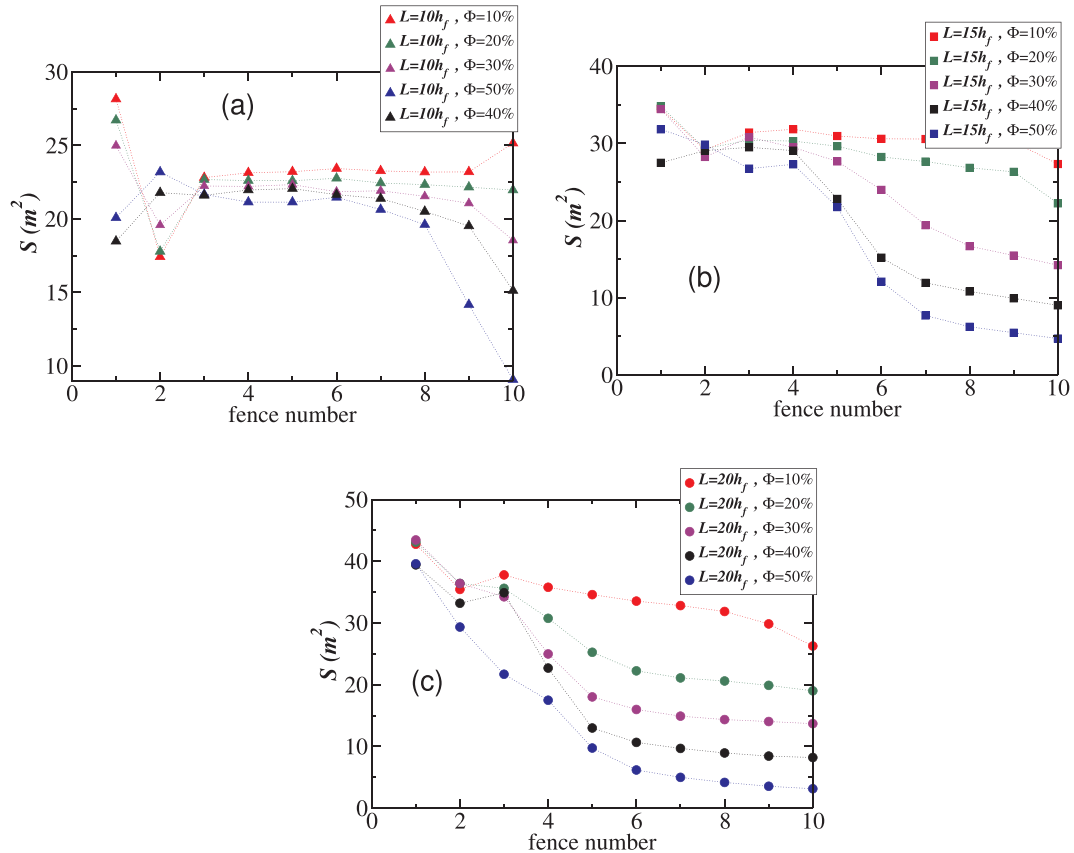


Fig. 9. Protected soil area S between two adjacent fences, i.e. the area within which $u_{sx} < u_{ft}$ ($= 0.25$ m/s), as a function of the fence position downwind for different values of the spacing and porosity. The area S is defined according to Eq. (5) and is rescaled by $S_0 = \Delta_y L$, which is the area between two adjacent fences.

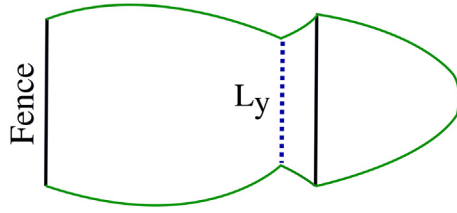


Fig. 10. Contour of the area S protected against aeolian entrainment in the two-fences experiment, obtained for $u_{*0} = 0.4$ m/s, $h_f = 50$ cm, $\phi = 40\%$ and $L_x = 20h_f$ (spacing). L_y denotes the smallest cross-wind width of the protected region between the fences.

B), which is separated from the upwind regime of inter-connected wake zones (regime A) at some point within the array depending on the inter-fence spacing.

3.3. Two-fence experiments elucidate the critical dependence of wake zones connectivity on inter-fence spacing

To investigate the dependence of the wake zones between adjacent fences on the spacing, described above, we perform systematic calculations of the protected soil area between an isolated pair of fences for different values of spacing. To this end, we perform a different type of numerical experiments in which only 2 fences are considered, while the spacing between both fences is systematically varied. The two fences have the same height, porosity and cross-wind width as the fences in the array considered in the previous calculations. Moreover, the wind tunnel has the same height and width Δy , and boundary conditions are the same as before. The only difference compared to the setup of Fig. 2 is the channel's downwind length, which is now $80h_f + L$.

Fig. 10 shows the contour plot of the wake zone from the upwind fence including the entire protected area associated with the downwind fence. In this particular calculation, the porosity is 40%, the fence height is 50 cm, the spacing is $10h_f$ and the upwind shear velocity is 0.4 m/s.

In Fig. 10, L_y denotes the smallest cross-wind width of the wake zone between the two fences. This cross-wind width decreases with the fence spacing L_x as shown in Fig. 11. We see from this figure that there is a critical value of L_x/h_f , which is slightly larger than 34, beyond which L_y is zero, i.e. the wake zones of the two fences are separated from each other. For larger values of the spacing ($\tilde{L}_x \equiv L_x/h_f \gtrsim 34$), the system is in the disconnected phase (regime B; $\tilde{L}_y \equiv L_y/h_f = 0$), while as

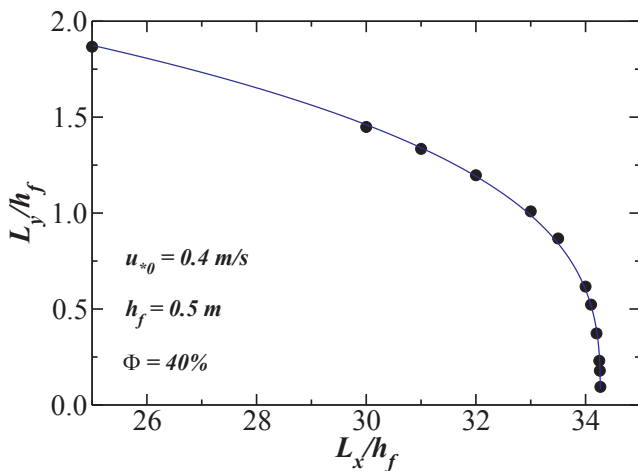


Fig. 11. Value of L_y defined in Fig. 10 as a function of the spacing between the fences, L_x , in the two-fences experiment. Both L_y and L_x are normalized by the fence height h_f . The filled circles denote our calculated data. The continuous line represents the best fit using Eq. (6), which gives $\tilde{L}_{xc} \approx 34.3$, $A \approx 2.85$ and $\beta \approx 0.32$.

the spacing decreases ($\tilde{L}_x \lesssim 34$), the system enters regime A, i.e. the connected phase ($\tilde{L}_y \neq 0$).

In the system of Fig. 11, the cross-wind width of the wake zone between the fences, L_y , goes to zero with a power law at $\tilde{L}_x = \tilde{L}_{xc}$ around 34 from regime B to regime A. We can describe the behavior of \tilde{L}_y by means of the following equation,

$$\tilde{L}_y = \begin{cases} A \cdot [1 - \tilde{L}_x/\tilde{L}_{xc}]^\beta, & \tilde{L}_x < \tilde{L}_{xc} \\ 0, & \tilde{L}_x \geq \tilde{L}_{xc} \end{cases} \quad (6)$$

where the critical point \tilde{L}_{xc} , the constant A and the exponent β can be determined from the best fit to the simulation data. The continuous line in Fig. 11 shows this best fit, which gives $\tilde{L}_{xc} \approx 34.3$, $A \approx 2.85$ and $\beta \approx 0.32$. The quality of the fit is remarkable. We thus conclude that the change in the system's behavior from regime A to regime B exhibits the characteristics of a second order phase transition at the critical spacing \tilde{L}_{xc} , where \tilde{L}_y represents an appropriate observable (order parameter) to describe this transition.

This behavior is similar, for instance, to the transition of percolation from the connected to the disconnected phase in random graphs (Herrmann and Roux, 1990), i.e., a set of objects that are randomly connected to each other. Specifically, in the generation of a random graph, for any pair of sites (or nodes) in the graph, a probability p is specified that these two sites are connected to each other. Accordingly, a probability $1 - p$ is defined that this pair of sites is disconnected or open. It can be shown that, when this microscopic probability p is defined above a given critical value p_c , the random graph is macroscopically connected in the sense that, to a probability P , a path can be identified that connects one extremity to the other in the entire assembly of nodes (i.e., percolation occurs to a probability P). However, when the probability p decreases below a critical value p_c , there is no connecting path and the random graph is said to be macroscopically disconnected (Herrmann and Roux, 1990; Stauffer and Aharony, 1994; Bunde and Havlin, 1996; Araújo et al., 2002; Parteli et al., 2010). It is interesting that the dependence of P on p for random graph percolation follows Eq. (6) with L_y/h_f in the role of P and L_x/h_f in the role of p . To the best of our knowledge, this is the first time that an equation reminiscent of random graph percolation theory is shown to describe a phase transition phenomenon in the structure of the wind flow over a terrain with fences. This finding can, thus, open up new ways to investigate the problem of aeolian flow structures over complex terrain topography from an analytical point of view in future work.

The results of our simulations are important for the drag partitioning schemes in models for aeolian surfaces with sand fences. In regime B, i.e., $\tilde{L}_x > \tilde{L}_{xc}$, the total drag can be then partitioned into a pressure drag, due to the momentum absorbed by the individual fences, and the surface drag on the underlying surface (Raupach, 1992). However, in regime A, i.e., $\tilde{L}_x < \tilde{L}_{xc}$, interactions of the turbulent wakes and mutual sheltering among the fences (see Fig. 8) lead to a reduction in the pressure drag on individual fences. In other words, as the density of the roughness elements (in the present study, the sand fences) increases, individual elements become less effective since only a fraction of them can be seen by the mean flow (Shao and Yang, 2005; Yang and Shao, 2006). As shown by Shao and Yang (2005), the effect of mutual sheltering between the roughness elements can be taken into account by including in the drag partitioning scheme by Raupach (1992) a third component, which is the skin drag due to momentum transfer to the surfaces of roughness elements (Shao and Yang, 2005; Yang and Shao, 2006).

However, it is interesting to discuss the disconnection of the wake zones between two adjacent fences within an array (cf. Fig. 8) in the light of the analysis made for two isolated fences in Figs. 10 and 11. In other words, these figures concern simulations of two fences, so the following question arises: How the results presented in these figures relate to multiple fence simulations? For a fence array, we have found that u_{*xc} , computed with Eq. (4), is increasing downwind, which means

that \tilde{L}_y decreases with distance downwind. The larger the spacing of the array, the earlier within the array the transition from regime A to regime B (disconnected wake zones) will occur, which means that the wind shear velocity is one important parameter controlling the critical spacing \tilde{L}_{xc} .

Therefore, considering, for instance, the array of 10 fences, qualitatively, the same behavior of the protected area as a function of interference spacing observed in Figs. 10 and 11 occurs for any pair of fences in the array, but the critical spacing for the transition between regimes A and B decreases with distance downwind. Moreover, in a given array, this critical spacing depends on several factors including the fence porosity and height, incident wind velocity and number of fences, since the disturbance of the boundary layer depends on the array's length and number of roughness elements (the fences). This dependence is, thus, worth investigating in more detail in future work. Moreover, the present study concerns a wind of constant velocity perpendicular to the fences, and thus further investigation is required to address realistic scenarios of wind velocity and direction variations. However, the analysis presented here represents a first step towards a complete description of the complex behavior of the protected soil area as a function of the geometric properties of an array of sand fences.

3.4. Multiple or constant fence heights?

In this subsection, we address the question whether combining fences of different heights may increase the efficiency of the fence array. Using the same amount of fence material, the aim is to find a combination of fence heights for which the reduction of near-surface wind shear velocity is optimal. To characterize this reduction, we consider the total amount of protected area (S) and we analyze different configurations of fences using two different heights, namely $h_f = 50$ cm and $h_f = 1$ m, defined as follows:

- setup A—fences of height $h_{f1} = 1.0$ m separated by a distance $10h_{f1}$ ($= 10$ m)
- setup B—fences of height $h_{f1} = 1.0$ m separated by pairs of fences of height $h_{f2} = 50$ cm, with constant spacing 6.67 m between all fences (see Fig. 12)
- setup C—fences of height $h_{f1} = 1.0$ m separated by pairs of fences of height $h_{f2} = 50$ cm, with spacing determined by the height of the upwind fence—in this setup, each pair of adjacent fences within the array is separated by a distance equal to 10 times the height of the upwind fence
- setup D—fences of height $h_{f2} = 50$ cm separated by a distance $10h_{f2}$ ($= 5$ m)

We note that the inter-fence spacing of 6.67 m in setup B was chosen to conserve the same amount of fence material (fence cross-sectional area) for the sake of comparison between all setups. Therefore, using setup B with the referred spacing leads to the same amount of fence material as in the other setups, for the same total target array's along-wind size.

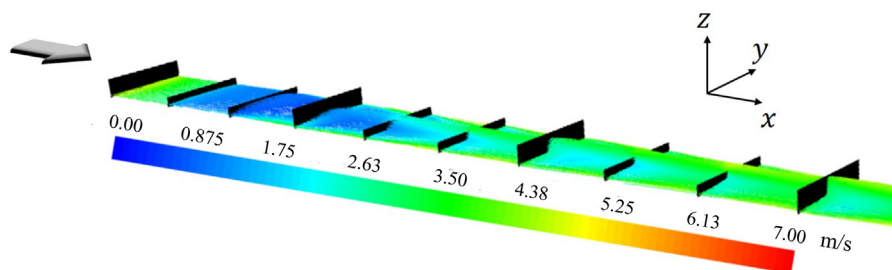


Fig. 12. Flow streamlines obtained for setup B, i.e. fences of height 1 m separated by pairs of fences of height 50 cm with constant spacing 6.67 m. The colors indicate the magnitude of the wind velocity in m/s. Upwind flow velocity $u_{s0} = 0.4$ m/s and fence porosity $\phi = 40\%$.

Fig. 13 shows the two-dimensional velocity field of the near-surface horizontal wind shear velocity $u_{sx}(x, y)$ (computed using Eq. (4)) for setups A-D, by using a fence porosity of 40% and upwind shear velocity 0.4 m/s. The total area S for which $u_{sx} < u_{ft}$ is calculated, as described in the previous subsection, as a function of the downwind position for all setups, and the result is shown in Fig. 14. In this figure, the area S produced by each fence is shown rescaled by the total area S_0 between the fence and its downwind neighbor. We can see that setup D, which uses constant fence height of 50 cm, produces larger values of S/S_0 compared to setup A (constant fence height of 1 m). Moreover, this figure shows that setups using multiple fence heights lead to intermediate efficiency between the two investigated setups of constant fence height—although at some few positions along the array, setups B and C locally produce lower S/S_0 than setup A and higher S/S_0 than D.

3.5. Wind velocity above the fences and interpretation of the simulation results in the light of experimental and field observations

In this study, we have adopted the definition introduced by Guan et al. (2009) for the near-surface wind shear velocity u_{sx} , computed from the wind velocity measured at a height of 20% of the fence height (Eq. (4)), to characterize the wind velocity field in the region between the fences. We have shown that, in the region between the fences, this u_{sx} is substantially smaller than the upwind wind shear velocity u_{s0} , and displays, after a transition zone that ends at the third fence, a slight increase downwind toward an asymptotic value far within the array—which is exactly the behavior observed in the experiments by Guan et al. (2009). Our numerical results agree, thus, with experimental observations, and we have also shown in Fig. 3 that the vertical profile of the horizontal velocity agrees reasonably well with the profile obtained experimentally (Guan et al., 2009). Therefore, we conclude that the model presented here can be applied in future work to investigate the flow properties of turbulent wind over porous fences.

However, while the computation of u_{sx} using the method by Guan et al. (2009) is useful to acquire quantitative information about the flow properties between porous fences, additional computations (specified next) are needed for application in sediment flux modelling and geomorphologic simulations. In particular, in the future our model should be adapted to investigate the two-dimensional field of the surface shear velocity u_{ss} obtained after the shear stress partition in the presence of the fences. Specifically, from this partition, the total shear stress τ can be written as $\tau = \tau_w + \tau_s$, where τ_w is the fraction of τ acting on the fences and τ_s is the surface shear stress, which acts on the grains, thus causing the sand flux, and is related to the surface shear velocity u_{ss} to the equation $\tau_s = \rho_{air} u_{ss}^2$.

The surface shear velocity u_{ss} can be obtained from the vertical profile of the horizontal wind velocity above the fences, within the disturbed boundary layer (i.e., within heights in the approximate range between 3 and 8 times the fence height; see Guan et al. (2009)). Although it is computationally expensive to perform a systematic investigation of the two-dimensional field $u_{ss}(x, y)$ using the model presented here, we investigated the behavior of the wind velocity for

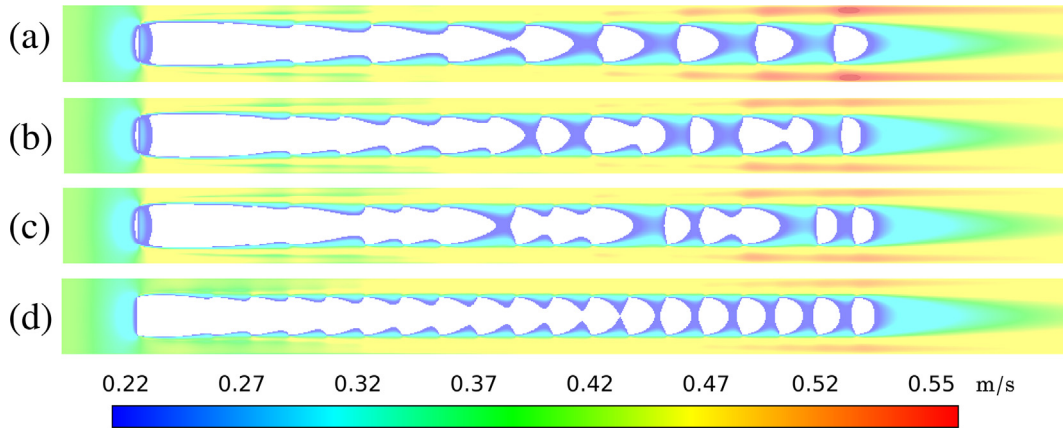


Fig. 13. Longitudinal component of the wind shear velocity field, u_{sx} , computed with Eq. (4), for the arrays of fences of setups A-D using multiple fence heights. *Setup A:* $h_f = 1.0$ m; *Setup B:* Alternating heights, homogeneous; *Setup C:* Alternating heights, heterogeneous; *Setup D:* $h_f = 50$ cm. The colors indicate the values of u_{sx} in m/s, with the white areas corresponding to u_{sx} values smaller than the minimal threshold for direct aerodynamic entrainment. The calculation results correspond to upwind flow velocity $u_{s0} = 0.4$ m/s and fence porosity $\phi = 40\%$, while fence height and inter-fence spacing are varied over the different setups as described in Section 3.4. There are different numbers of fences in the different setups, as discussed in the text of subSection 3.4, since the spacing between fences i and $i + 1$ is equal to 10 times the height of fence i . The wind shear velocity has been calculated at height $z = 10$ cm using Eq. (4).

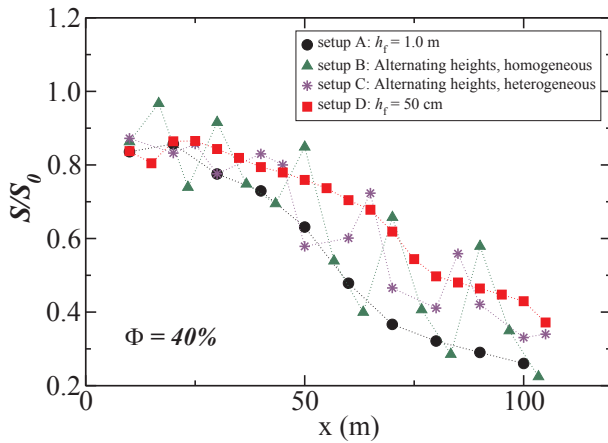


Fig. 14. Area S of soil between adjacent fences associated with near-surface wind shear velocity below the minimal threshold for direct aeolian entrainment as a function of the downwind position, computed for the different setups A-D using multiple fence heights. The points in each curve correspond to the fences $i = 1 \dots N$ in the respective setups A-D, while S is the protected area between fence i and $i + 1$, i.e. the area between the adjacent fences within which $u_{sx} < u_{s0}$. Moreover, S_0 represents the total area $\Delta y \cdot L_i$ between fences i and $i + 1$.

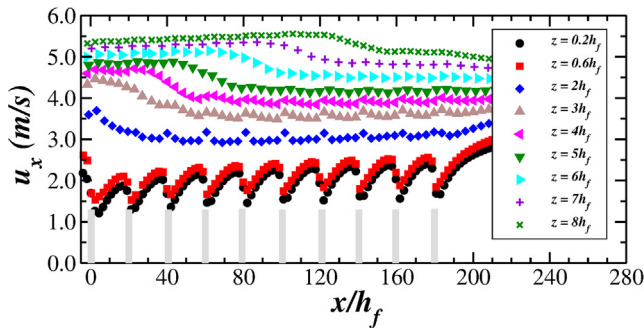


Fig. 15. Wind velocity in the longitudinal direction at $y = 0$, i.e., along the symmetry axis of the fence array, computed at different heights z . The vertical line segments raised from the graph's baseline have been introduced as guide-to-the-eye, for representing the position of the fences. The fences have porosity 40% and height 50 cm, and upwind shear velocity is 0.40 m/s.

various values of the downwind position along the symmetry axis of the fence array and at different heights above the ground, including heights above the array of fences. As can be seen in Fig. 15, while the maximal values of wind speed near the surface within the region between the fences (i.e., $z < h_f$) increase slowly with the distance downwind (as demonstrated experimentally by Guan et al. (2009)), above the fences, u_x displays a different behavior. Specifically, far downwind within the array, the wind velocity above the fences decreases with x . This behavior is consistent with experimental observations, which show that the wind speed above a very long array of fences decreases with x towards an asymptotic value (Guan et al., 2009).

Moreover, Gillies et al. (2007) performed field measurements of the surface shear stress, τ_s , for roughness configurations made of solid elements in staggered arrays of different roughness densities. To obtain the surface shear stress on the ground between the elements (τ_s), Gillies et al. (2007) employed Irwin sensors, which consist of simple, omnidirectional skin frictionmeters that measure the near-surface vertical pressure gradient. Moreover, Gillies et al. (2017) presented field investigation of the sand flux on a terrain with porous sand fences, while Gillies et al. (2018) performed a field study of the sand flux over a terrain of roughness elements. In both studies, it was found that the sand flux over the soil with the obstacles (porous fences or roughness elements) decreases downwind toward an asymptotic value. Since the sand flux responds to the surface shear stress τ_s , it would be thus interesting to extend our two-dimensional field computations and the study of wake zone percolation presented here to the investigation of this surface shear stress in the presence of various types of obstacles and array configurations.

In summary, we have found that the wind velocity u_x within the disturbed boundary layer above an array of porous fences decreases with distance downwind as found in the experiments by Guan et al. (2009). However, the results of Fig. 15 indicate that longer arrays than the ones used in our simulations are needed to assess the convergence of the wind velocity towards its asymptotic value downwind. Moreover, our model must be improved to efficiently compute $u_{sx}(x, y)$ over the simulation domain. Alternatively, the simulation of Irwin sensors, employed in previous field work (Gillies et al., 2017), could be developed to directly obtain the surface shear stress τ_s building on the CFD model presented here.

Our study is the first to report a second-order phase transition associated with the average turbulent wind field over a terrain with windbreaks, thus providing new insights for future theoretical work on this topic. We hope that the present study will motivate future

investigation on the effect of different system parameters on the area S for which the near-surface wind shear velocity is below the minimal threshold for direct entrainment, as well as on the critical rescaled distance \tilde{L}_{xc} , the constant A and the exponent β in Eq. (6). Moreover, it would be interesting to verify our prediction for the phase transition in Eq. (6) by means of field measurements or wind tunnel experiments.

4. Conclusions and outlook

We performed three-dimensional CFD simulations of the average turbulent wind field over a flat terrain in presence of an array of porous fences. The calculations were performed with different values for porosity, height and spacing, and the present work focused on the total area S of sediment soil for which the near-surface wind shear velocity, defined in the airflow model by Guan et al. (2009) (Eq. (4)) is smaller than the minimal threshold for direct aerodynamic entrainment. We found that there is a critical inter-fence spacing L_{xc} that separates two regimes of behavior: For $L_x > L_{xc}$, the wake zones of the different fences in the array are disconnected (regime B), while for $L_x < L_{xc}$, no separation occurs between zones of wind shear velocity below threshold (regime A). We find that the system undergoes a continuous phase transition from regime B to regime A as L_x decreases below L_{xc} . In regime A, the cross-wind width of the protected zone, L_y (the order parameter) scales with $(1 - L_x/L_{xc})^\beta$, where the exponent β is around 0.32.

Moreover, we have analyzed the influence of fence's height and porosity on the fluid structure. Our simulations have shown that an array of 50 cm high fences performs better, with regard to the total area S , than counterparts containing 1 m high fences or fence heights alternating between 50 cm and 1 m. We note that scenario D ($h_f = 50$ cm) has twice as large number of fences as in scenario A ($h_f = 1$ m). Although the area shielded by a single fence in setup A is larger than in setup D, our simulations show that, collectively, the smaller counterparts produce a higher relative area S/S_0 associated with below-threshold u_{*x} . This finding is interesting because the experimental realization of scenarios A and D are associated with the same amount of fence material. However, this finding also raises interesting questions, as for instance, what happens if even smaller values of h_f are used, which deserve to be addressed in simulations and experiments following the present work. However, in practice, preference is given to fences of height as large as possible, given that maintenance and renewal of the windbreaks is regularly needed following processes of sand deposition and dune formation induced by wind velocity reduction over the array (Li and Sherman, 2015).

Furthermore, we have found that, along the flanks of the fence array, the along-wind component of the near-surface wind shear velocity u_{*x} is largest and increases linearly with distance downwind. In particular, u_{*x} exceeds the upwind value u_{*0} after the third fence. Our simulations have shown that the increase in flow velocity at the lateral borders is stronger the higher the porosity, since the pressure drop at the sides of the fence array is stronger the less permeable the fences.

The techniques we investigated in the present manuscript have impact on man-made geomorphology. Specifically, the investigation performed in our work is concerned with an intervention that is designed to prevent soil erosion, i.e. the erection of sand fences to reduce the local wind speed below the minimal value for sediment transport. One outlook of the present work would be the simulation of the soil topography in presence of the fences. Such simulations can be achieved by coupling the CFD modeling presented here with the morphodynamic model for aeolian landscapes developed in the last years (Sauermann et al., 2001; Kroy et al., 2002; Sauermann et al., 2003; Parteli et al., 2006; Herrmann et al., 2008; Durán et al., 2010; Parteli et al., 2011; Luna et al., 2009; Luna et al., 2011; Luna et al., 2012; Melo et al., 2012; Parteli et al., 2014; Parteli et al., 2019; Muchowski et al., 2019).

Moreover, many open questions remain to be investigated in the

future, such as how the predictions reported here change if intermittent transport conditions that occur in real field scenarios (Ellis et al., 2012; Sherman et al., 2013) are considered. Moreover, one further aspect to be incorporated in future studies is the effect of the stochastic nature of turbulence on the threshold for sand and dust emission. Accurately modeling such forces is a difficult task that is still matter of intense research (Klose and Shao, 2012), and is important to correctly represent threshold wind speeds for sediment entrainment (Kok et al., 2012; Li et al., 2014). Large-scale arrays of sand fences disposed in different ways, such as in zig-zag (Bitog et al., 2009) or checkerboards (Qiu et al., 2004), should be also modeled in future works.

In this context, we remark that Xu et al. (2018) pioneered the study of the flow characteristics of turbulent aeolian sand over straw checkerboard barriers and the erosion-deposition patterns resulting from the interaction between particles, fluid and obstacles. In particular, these authors studied the flow over checkerboards by taking into account the motion of the particles, which disturb the wind profile (Xu et al., 2018). In their simulations, the checkerboards consisted of 10 cm high obstacles, and wind tunnel experiments were also performed using the same conditions as in the simulations to verify the predictions for wind velocity and sand flux (Xu et al., 2018). The model by Xu et al. (2018) is, thus, different from ours, since we investigate the structure of the flow without particles. It is, thus, not possible to apply the same technique proposed by Xu et al. (2018) to validate the simulation predictions for vertical sand flux profile, since in our simulations we only investigated the structure of the turbulent wind free of saltating or suspended particles. Moreover, with regard to a verification of the wind profile alone (without particles), to the best of our knowledge, there is no experiment that investigates the turbulent flow profile using the same conditions as in our simulations. However, the longitudinal profile of the wind shear velocity we have presented in our manuscript matches very well the trend observed in the experiments by Guan et al. (2009). We remark that the study of the flow without particles is important as a preliminary investigation to the sand flux, since the turbulent wind flow has still many complex aspects that are still poorly understood—one of these aspects is the average shape of the zones with no aerodynamic entrainment as a function of the inter-fence distance, investigated in our manuscript.

We hope that the predictions made from the simulations presented here will trigger field work to verify our results, as well as further effort toward optimization of strategies to protect soil erosion with sand fences.

CRedit authorship contribution statement

Izrael A. Lima: Conceptualization, Methodology, Software, Validation, Formal analysis, Investigation, Writing - review & editing. **Eric J.R. Parteli:** Conceptualization, Methodology, Validation, Formal analysis, Investigation, Writing - original draft. **Yaping Shao:** Conceptualization, Methodology, Formal analysis, Investigation, Writing - review & editing. **José S. Andrade:** Conceptualization, Methodology, Investigation, Writing - review & editing. **Hans J. Herrmann:** Conceptualization, Methodology, Investigation, Writing - review & editing. **Ascânio D. Araújo:** Conceptualization, Methodology, Validation, Formal analysis, Investigation, Writing - review & editing.

Declaration of Competing Interest

The authors declare that they have no known competing financial interests or personal relationships that could have appeared to influence the work reported in this paper.

Acknowledgements

This work was supported in part by CAPES, CNPq and FUNCAP (Brazilian agencies), the Brazilian Institute INCT-SC, by the German

Research Foundation (DFG) Grant RI 2497/7-1 and by ERC Advanced grant FP7-319968 FlowCCS of the European Research Council.

Appendix A. Supplementary data

Supplementary data associated with this article can be found, in the online version, at <https://doi.org/10.1016/j.aeolia.2020.100574>.

References

- Alhajraf, S., 2004. Computational fluid dynamic modeling of drifting particles at porous fences. *Environ. Model. Softw.* 19, 163–170.
- Almeida, M.P., Andrade Jr., J.S., Herrmann, H.J., 2006. Aeolian transport layer. *Phys. Rev. Lett.* 96, 018001.
- Almeida, M.P., Parteli, E.J.R., Andrade Jr., J.S., Herrmann, H.J., 2008. Giant saltation on Mars. *Proc. Natl. Acad. Sci.* 105, 6222–6226.
- Araújo, A.D., Andrade Jr., J.S., Maia, L.P., Herrmann, H.J., 2009. Numerical simulation of particle flow in a sand trap. *Granul. Matter* 11, 193–200.
- Araújo, A.D., Moreira, A.A., Makse, H.A., Stanley, H.E., Andrade Jr., J.S., 2002. Traveling length and minimal traveling time for flow through percolation networks with long-range spatial correlations. *Phys. Rev. E* 66, 046304.
- Araújo, A.D., Parteli, E.J.R., Pöschel, T., Andrade Jr., J.S., Herrmann, H.J., 2013. Numerical modeling of the wind flow over a transverse dune. *Scientific Rep.* 3, 2858.
- Bagnold, R.A., 1941. *The Physics of Blown Sand and Desert Dunes*. Methuen, London.
- Baltare, R., 1967. Air flow patterns in the lee of model windbreaks. *Arch. Meteorol. Geophys. Bioklimatol. Ser. B* 15, 3.
- Bitog, J.P., Lee, I.B., Shin, M.H., Hong, S.W., Hwang, H.S., Seo, I.H., Yoo, J.I., Kwon, K.S., Kim, Y.H., Han, J.W., 2009. Numerical simulation of an array of fences in Saemangeum reclaimed land. *Atmos. Environ.* 43, 4612–4621.
- Bouvet, T., Wilson, J.D., Tuzet, A., 2006. Observations and modeling of heavy particle deposition in a windbreak flow. *J. Appl. Meteorol. Clim.* 45, 1332–1349.
- Bruno, L., Fransos, D., Lo Giudice, A., 2018. Solid barriers for windblown sand mitigation: aerodynamic behavior and conceptual design guidelines. *J. Wind Eng. Ind. Aerodyn.* 173, 79–90.
- Bunde, A., Havlin, S., 1996. *Fractals and Disordered Systems*. Springer, Berlin-Heidelberg.
- Carneiro, M.V., Araújo, N.A.M., Pähz, T., Herrmann, H.J., 2013. Mid-air collisions enhance saltation. *Phys. Rev. Lett.* 111, 058001.
- Carneiro, M.V., Pähz, T., Herrmann, H.J., 2011. Jump at the onset of saltation. *Phys. Rev. Lett.* 107, 098001.
- Claudin, P., Wiggs, G.F.S., Andreotti, B., 2013. Field evidence for the upwind velocity shift at the crest of low dunes. *Bound.-Layer Meteorol.* 148, 195–206.
- Cornelis, W.M., Gabriels, D., 2005. Optimal windbreak design for wind-erosion control. *J. Arid Environ.* 61, 315–332.
- Dong, Z., Qian, G., Luo, W., Wang, H., 2006. Threshold velocity for wind erosion: the effects of porous fences. *Environ. Geol.* 51, 471–475.
- Durán, O., Parteli, E.J.R., Herrmann, H.J., 2010. A continuous model for sand dunes: review, new developments and application to barchan dunes and barchan dune fields. *Earth Surf. Proc. Landforms* 35, 1591–1600.
- Ellis, J.T., Sherman, D.J., Farrell, E.J., Li, B., 2012. Temporal and spatial variability of aeolian sand transport: implications for field measurements. *Aeolian Res.* 3, 379–387.
- Gillies, J., Etyemezian, V., Nikolich, G., Nickling, W.G., Kok, J., 2018. Changes in the saltation flux following a step-change in macro-roughness. *Earth Surf. Proc. Land.* 43, 1871–1884.
- Gillies, J.A., Etyemezian, V., Nikolich, G., Glick, R., Rowland, P., Pesce, T., Skinner, M., 2017. Effectiveness of an array of porous fences to reduce sand flux: Oceano Dunes, Oceano CA. *J. Wind Eng. Ind. Aerodyn.* 168, 247–259.
- Gillies, J.A., Nickling, W.G., King, J., 2007. Shear stress partitioning in large patches of roughness in the atmospheric inertial sublayer. *Bound.-Layer Meteorol.* 122, 367–396.
- Guan, D.X., Zhong, Y., Jin, C.J., Wang, A.Z., Wu, J.B., Shi, T.T., Zhu, T.Y., 2009. Variation in wind speed and surface shear stress from open floor to porous parallel windbreaks: a wind tunnel study. *J. Geophys. Res.* 114, D15106.
- Hatanaka, K., Hotta, S., 1997. Finite element analysis of air flow around permeable sand fences. *Int. J. Numer. Meth. Fl.* 24, 1291–1306.
- Herrmann, H.J., Andrade Jr., J.S., Schatz, V., Sauer mann, G., Parteli, E.J.R., 2005. Calculation of the separation streamlines of barchans and transverse dunes. *Phys. A* 357, 44–49.
- Herrmann, H.J., Durán, O., Parteli, E.J.R., Schatz, V., 2008. Vegetation and induration as sand dunes stabilizers. *J. Coastal Res.* 24, 1357–1368.
- Herrmann, H.J., Roux, S., 1990. *Statistical Models for the Fracture of Disordered Media*. Elsevier Science Publishers B.V. (North-Holland).
- Klose, M., Shao, Y., 2012. Stochastic parameterization of dust emission and application to convective atmospheric conditions. *Atmos. Chem. Phys.* 12, 7309.
- Kok, J.F., Parteli, E.J.R., Michaels, T.I., Bou Karam, D., 2012. The physics of wind-blown sand and dust. *Rep. Prog. Phys.* 75, 106901.
- Kroy, K., Sauer mann, G., Herrmann, H.J., 2002. Minimal model for aeolian sand dunes. *Phys. Rev. E* 66, 031302.
- Launder, B.E., Spalding, D.B., 1974. The numerical computation of turbulent flows. *Comput. Method. Appl. Mech.* 3, 269–289.
- Lee, S.J., Kim, H.B., 1999. Laboratory measurements of velocity and turbulence field behind porous fences. *J. Wind Eng. Ind. Aerod.* 80, 311–326.
- Lee, S.J., Lim, H.C., 2001. A numerical study on flow around a triangular prism located behind a porous fence. *Fluid Dyn. Res.* 28, 209–221.
- Lee, S.J., Park, K.C., 2002. Wind tunnel observations about the shelter effect of porous fences on the sand particle movements. *Atmos. Environ.* 36, 1453–1463.
- Li, B., Ellis, J.T., Sherman, D.J., 2014. Estimating the impact threshold for wind-blown sand. *J. Coastal Res.* 70, 627–632.
- Li, B., Sherman, D.J., 2015. Aerodynamics and morphodynamics of sand fences: a review. *Aeolian Res.* 17, 33–48.
- Lima, I.A., Araújo, A.D., Parteli, E.J.R., Andrade, J.S., Herrmann, H.J., 2017. Optimal array of sand fences. *Scientific Rep.* 7, 45148.
- Liu, B., Qu, J., Zhang, W., Tan, L., Gao, Y., 2014. Numerical evaluation of the scale problem on the wind flow of a windbreak. *Scientific Rep.* 4, 6619.
- Lu, H., Shao, Y., 1999. A new model for dust emission by saltation bombardment. *J. Geophys. Res.* 104, 16827–16842.
- Luna, M.C.M.M., Parteli, E.J.R., Durán, O., Herrmann, H.J., 2009. Modeling transverse dunes with vegetation. *Phys. A* 388, 4205–4217.
- Luna, M.C.M.M., Parteli, E.J.R., Durán, O., Herrmann, H.J., 2011. Model for the genesis of coastal dune fields with vegetation. *Geomorphology* 129, 215–224.
- Luna, M.C.M.M., Parteli, E.J.R., Herrmann, H.J., 2012. Model for a dune field with an exposed water table. *Geomorphology* 159–160, 169–177.
- Melo, H.P.M., Parteli, E.J.R., Andrade, J.S., Herrmann, H.J., 2012. Linear stability analysis of transverse dunes. *Phys. A* 391, 4606–4614.
- Michelsen, B., Strobl, S., Parteli, E.J.R., Pöschel, T., 2015. Two-dimensional airflow modeling underpredicts the wind velocity over dunes. *Scientific Rep.* 5, 16572.
- Muchowski, J., Griewank, P.J., Shao, Y., Parteli, E.J.R., 2019. Atmospheric boundary layer flow at the sand interface. In: Poster presented at the 6th Conference of the Graduate School of Geosciences at the University of Cologne, Germany.
- Nordstrom, K.F., Jackson, N.L., Freestone, A.L., Korotky, K.H., Puleo, J.A., 2012. Effects of beach raking and sand fences on dune dimensions and morphology. *Geomorphology* 179, 106–115.
- Pähz, T., Durán, O., 2018. The cessation threshold of nonsuspended sediment transport across aeolian and fluvial environments. *J. Geophys. Res.*
- Pähz, T., Kok, J.F., Parteli, E.J.R., Herrmann, H.J., 2013. Flux saturation length of sediment transport. *Phys. Rev. Lett.* 111, 218002.
- Park, C.W., Lee, S.J., 2003. Experimental study on surface pressure and flow structure around a triangular prism located behind a porous fence. *J. Wind Eng. Ind. Aerodyn.* 91, 165–184. Fifth Asia-Pacific Conference on Wind Engineering.
- Parteli, E.J.R., Andrade Jr., J.S., Herrmann, H.J., 2011. Transverse instability of dunes. *Phys. Rev. Lett.* 107, 188001.
- Parteli, E.J.R., da Silva, L.R., Andrade Jr., J.S., 2010. Self-organized percolation in multi-layered structures. *J. Stat. Mech: Theory Exp.* P03026.
- Parteli, E.J.R., Kroy, K., Tsoar, H., Andrade Jr., J.S., Pöschel, T., 2014. Morphodynamic modeling of aeolian dunes: review and future plans. *Eur. Phys. J. Spec. Top.* 223, 2269–2283.
- Parteli, E.J.R., Lima, I.A., Muchowski, J., Shao, Y., Andrade Jr., J., Herrmann, H.J., Araújo, A.D., Kryger, M., 2019. Turbulent wind flow and sediment transport over a terrain with sand fences: coupled simulations using cfd and a morphodynamic model. In: *European Geosciences Union General Assembly 2019*. Abstract 9598.
- Parteli, E.J.R., Schwämmle, V., Herrmann, H.J., Monteiro, L.H.U., Maia, L.P., 2006. Profile measurement and simulation of a transverse dune field in the lençois Maranhenses. *Geomorphology* 81, 29–42.
- Patankar, S.V., Spalding, D.B., 1972. A calculation procedure for heat, mass and momentum transfer in three-dimensional parabolic flows. *Int. J. Heat Mass Transfer* 15, 1787–1806.
- Pye, K., Tsoar, H., 1990. *Aeolian Sand and Sand Dunes*. Uwin Hyman, London.
- Qiu, G.Y., Lee, I.B., Shimizu, H., Gao, Y., Ding, G., 2004. Principles of sand dune fixation with straw checkerboard technology and its effects on the environment. *J. Arid Environ.* 56, 449–464.
- Raupach, M.R., 1992. Drag and drag partition on rough surfaces. *Boundary-Layer Meteorol.* 60, 374–396.
- Santiago, J.L., Martín, F., Cuerva, A., Bezdeneznykh, N., Sanz-Andrés, A., 2007. Experimental and numerical study of wind flow behind windbreaks. *Atmos. Environ.* 41, 6406–6420.
- Sauer mann, G., Andrade Jr., J.S., Maia, L.P., Costa, U.M.S., Araújo, A.D., Herrmann, H.J., 2003. Wind velocity and sand transport on a barchan dune. *Geomorphology* 54, 245–255.
- Sauer mann, G., Kroy, K., Herrmann, H.J., 2001. A continuum saltation model for sand dunes. *Phys. Rev. E* 64, 31305.
- Savage, R.P., 1963. Experimental study of dune building with sand fences. In: *Coastal Engineering 1962, Proceedings of the 8th International Conference*, Mexico City. American Society of Civil Engineers, Mexico.
- Schatz, V., Herrmann J., H., 2006. Flow separation in the lee side of transverse dunes: A numerical investigation. *Geomorphology* 81 (1–2), 207–216. <https://doi.org/10.1016/j.geomorph.2006.04.009>.
- Shao, Y., 2001. A model for mineral dust emission. *J. Geophys. Res.* 106, 20239–20254.
- Shao, Y., 2008. *Physics and Modelling of Wind Erosion*. Springer Science & Business Media.
- Shao, Y., Li, A., 1999. Numerical modelling of saltation in the atmospheric surface layer. *Bound.-Layer Meteorol.* 91, 199–225.
- Shao, Y., Raupach, M.R., Findlater, P.A., 1993. Effect of saltation bombardment on the entrainment of dust by wind. *J. Geophys. Res.* 12, 12719–12726.
- Shao, Y., Yang, Y., 2005. A scheme for drag partition over rough surfaces. *Atmos. Environ.* 39, 7351–7361.
- Sherman, D.J., Li, B., Ellis, J.T., Farrell, E.J., Maia, L.P., Granja, H., 2013. Recalibrating aeolian sand transport models. *Earth Surf. Proc. Landforms* 38, 169–178.
- Stauffer, D., Aharony, A., 1994. *Introduction to Percolation Theory*. CRC Press, London.
- Telenta, M., Duhovnik, J., Kosel, F., Šajin, V., 2014. Numerical and experimental study of the flow through a geometrically accurate porous wind barrier model. *J. Wind Eng.*

- Ind. Aerodyn. 124, 99–108.
- Tsoar, H., 2001. Types of aeolian sand dunes and their formation. *Lect. Notes Phys.* 582, 403–429.
- Tsukahara, T., Sakamoto, Y., Aoshima, D., Yamamoto, M., Kawaguchi, Y., 2012. Visualization and laser measurements on the flow field and sand movement on sand dunes with porous fences. *Exp. Fluids* 52, 877–890.
- Wasson, R.J., Hyde, R., 1983. Factors determining desert dune type. *Nature* 304, 337–339.
- Wilson, J.D., 1985. Numerical studies of flow through a windbreak. *J. Wind Eng. Ind. Aerod.* 21, 119–154.
- Wilson, J.D., 1987. On the choice of a windbreak porosity profile. *Boundary-Lay. Meteorol.* 38, 37–49.
- Wilson, J.D., 2004. Oblique, stratified winds about a shelter fence. Part II: comparison of measurements with numerical models. *J. Appl. Meteorol.* 43, 1392–1409.
- Wu, X., Zou, X., Zhang, C., Wang, R., Zhao, J., Zhang, J., 2013. The effect of wind barriers on airflow in a wind tunnel. *J. Arid Environ.* 97, 73–83.
- Xu, B., Zhang, J., Huang, N., Gong, K., Liu, Y., 2018. Characteristics of turbulent aeolian sand movement over straw checkerboard barriers and formation mechanisms of their internal erosion form. *J. Geophys. Res.: Atmospheres* 123, 6907–6919.
- Yang, Y., Shao, Y., 2006. A scheme for scalar exchange in the urban boundary layer. *Boundary-Lay.-Meteorol.* 120, 111–132.
- Yeh, C.P., Tsai, C.H., Yang, R.J., 2010. An investigation into the sheltering performance of porous windbreaks under various wind directions. *J. Wind Eng. Ind. Aerodyn.* 98, 520–532.
- Zhang, N., Lee, S.J., Chen, T.G., 2015. Trajectories of saltating sand particles behind a porous fence. *Geomorphology* 228, 608–616.